



**HAL**  
open science

## Experimental and Numerical Studies in a Centrifugal Pump With Two-Dimensional Curved Blades in Cavitating Condition

Olivier Coutier-Delghosa, Regiane . Fortes Patella, Jean-Luc Reboud, Mickael Hofmann, Bernd Stoffel

► **To cite this version:**

Olivier Coutier-Delghosa, Regiane . Fortes Patella, Jean-Luc Reboud, Mickael Hofmann, Bernd Stoffel. Experimental and Numerical Studies in a Centrifugal Pump With Two-Dimensional Curved Blades in Cavitating Condition. Journal of Fluids Engineering, 2003, 125 (6), pp.970-978. 10.1115/1.1596238 . hal-00211209

**HAL Id: hal-00211209**

**<https://hal.science/hal-00211209>**

Submitted on 3 Jan 2020

**HAL** is a multi-disciplinary open access archive for the deposit and dissemination of scientific research documents, whether they are published or not. The documents may come from teaching and research institutions in France or abroad, or from public or private research centers.

L'archive ouverte pluridisciplinaire **HAL**, est destinée au dépôt et à la diffusion de documents scientifiques de niveau recherche, publiés ou non, émanant des établissements d'enseignement et de recherche français ou étrangers, des laboratoires publics ou privés.



Distributed under a Creative Commons Attribution 4.0 International License

# Experimental and Numerical Studies in a Centrifugal Pump With Two-Dimensional Curved Blades in Cavitating Condition

O. Coutier-Delgosha<sup>1</sup>

R. Fortes-Patella

J. L. Reboud<sup>2</sup>

Laboratoire des Ecoulements,  
Géophysiques et Industriels,  
B. P. 53,  
Grenoble, 38041, France

M. Hofmann

B. Stoffel

Laboratory for Turbomachinery and Fluid Power,  
Darmstadt University of Technology,  
Darmstadt D-64289, Germany

*In the presented study a special test pump with two-dimensional curvature blade geometry was investigated in cavitating and noncavitating conditions using different experimental techniques and a three-dimensional numerical model implemented to study cavitating flows. Experimental and numerical results concerning pump characteristics and performance breakdown were compared at different flow conditions. Appearing types of cavitation and the spatial distribution of vapor structures within the impeller were also analyzed. These results show the ability of the model to simulate the complex three-dimensional development of cavitation in a rotating machinery, and the associated effects on the performance.*

## 1 Introduction

The work presented in this paper was carried out in the scope of the European Research Program PROCOPE, between researchers of the TUD (Darmstadt University of Technology, Laboratory for Turbomachinery and Fluid Power) and of the LEGI (Laboratoire des Ecoulements Géophysiques et Industriels de Grenoble). The aim of this European program was to improve the understanding of the unsteady behavior of cavitating flows and the related erosive aggressiveness by experimental analyses and development of numerical models.

In this context, some research works were developed by both laboratories to analyze and to characterize erosion phenomenon, [1,2], as well as to study and to model unsteady cavitating flows around a two-dimensional hydrofoil, [3], and in a cascade of three hydrofoils, [4].

In order to extend those previous analyses, the present study consists of investigations by experimental means and numerical simulation of a special centrifugal test pump in cavitating and noncavitating conditions. Experiments were carried out at the TUD using different experimental techniques. The measurement of classical pump characteristics and performance breakdown at different flow conditions were associated with flow visualisations. Appearing types of cavitation and the spatial distribution of vapor structures within the impeller were analyzed.

Three-dimensional Navier-Stokes codes taking into account the cavitation process have been developed during the last years, [5–8], based on different multiphase flow approaches, [9,10]. Industrial CFD codes are now starting to take into account cavitation models, allowing first applications to pump geometries, [11,12]. In this context, a numerical model for three-dimensional cavitating flows is developed at LEGI, based on the three-dimensional code FINE/TURBO™, developed by NUMECA International. This work is performed in cooperation with the Rocket Engine Division of SNECMA Moteurs and the French Space Agency CNES, with the final objective to provide accurate simulations of unsteady cavitating flows in the inducers of rocket

engine turbopumps, [13,14]. The application to the centrifugal pump represents a first step of validation of the model on steady-state cavitating flow in turbomachinery.

## 2 Geometry

A special impeller geometry has been chosen to easily adapt existing measuring techniques for a single hydrofoil in a test section, [3,15], to a pump test rig. Optical access in two planes was made possible to enable a view perpendicular to the blade surface on both suction and pressure side by Plexiglas windows in the housing and a Plexiglas shroud. The impeller has five single-curved blades with two different radii at inlet and outlet. The part of the blade with the larger radius (the second part in flow direction) was also made of Plexiglas to obtain optical access to the pressure side of the following blade and the entire channel, respectively.

Figure 1(a) shows the intersection of the two blade radii. Another characteristic is the parallel hub and shroud to get an almost two-dimensional blade-to-blade channel with constant width. An axial-symmetric housing (Fig. 1(b)) is used to obtain almost constant conditions at the impeller outlet (if we neglect gravitational forces that are small compared to the performance of the impeller). With these preconditions we obtain comparable cavitation conditions in each channel without the influence of a volute casing.

Nominal conditions are at a rotational speed of 36 Hz and a flow rate  $Q = 210 \text{ m}^3/\text{h}$ . Specific speed of the impeller is  $n_s = nQ^{1/2}/H^{3/4} = 20$  (European units:  $n_s$  and  $n$  in rpm,  $Q$  in  $\text{m}^3/\text{s}$  and  $H$  in m), the outer impeller diameter equals 278 mm. Cavitation conditions are defined by NPSH value based on the upstream total pressure, water vapor pressure and density at ambient temperature.

## 3 Visualizations

Besides the measurements of the characteristics of the pump at different flow-rates and cavitation conditions, various visualization techniques were used. All images shown in this paper were taken at nominal flow rate with various values of NPSH, where both cavitation on suction and pressure side of the blades occurs.

Stroboscopic light was used on one hand for standard imaging and high-speed video with the light-sheet illumination (Fig. 2) was applied to observe self-oscillating states of the cavitation on the blade pressure side or other unsteady effects, [16].

<sup>1</sup>Currently at ENSTA UME/DFA, chemin de la Huniere, 91761 Palaiseau cedex, France.

<sup>2</sup>Currently at LTDS/ENISE, Saint-Etienne, France.

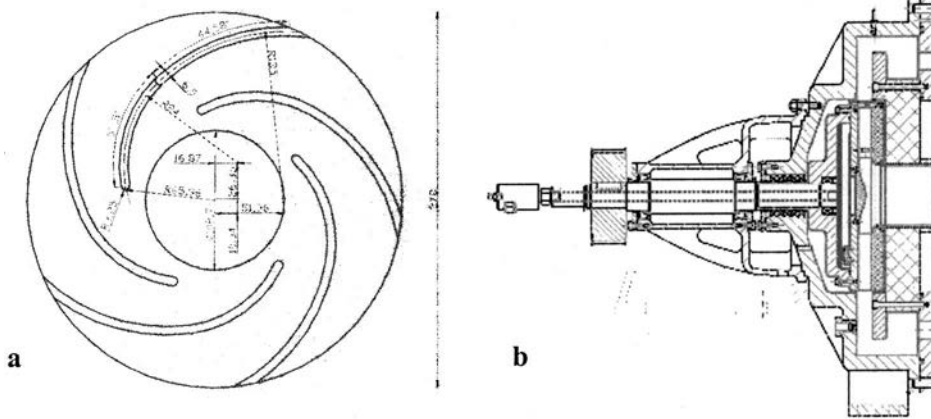


Fig. 1 (a) Impeller geometry, (b) housing

The investigated flow conditions during the experiments show always unsteady behavior of the leading-edge cavitation, not only concerning the unsteadiness of the closure region of the attached cavitation but also the shedding of vapor structures in the channel. Besides the well-known attached cavitation on pressure and suction side, another type of cavitation occurs at the inlet of the impeller caused by the strong curvature of the streamlines along the front shroud. It is visible either as attached cavitation caused by the depression at the radius (regions B and C in Fig. 3), or as shear cavitation because the flow was separating at the inlet radius of the front shroud at lower values of NPSH (region B in Fig. 4). Dependent on the length of the attached part of the cavitation (region A in all figures) the extent of this shear layer cavitation spreads into the channel as it is shown in Fig. 4 at two different stages of a cavitation cycle. In Fig. 4(a) the larger extent of the shear cavitation (region B) on top of the attached part (see region A, the illuminated interface of the cavitation sheet on the pressure side) is visible. In Fig. 4(b) (with a smaller cavitation sheet) no shear cavitation can be seen. The contour of the interface of the attached part of the cavitation (region A) already indicates a different state of the typical self-oscillating cloud cavitation condition.

With the aid of laser light-sheet illumination of the vapor-fluid interface, an analysis of the unsteadiness of the attached part of the cavitation in the impeller could be done at half-width of the channel. The images were taken at a rate of 2 Hz but triggered by an angular encoder and a special signal conditioning that allowed

to take the image at every phase angle compared to a reference angle with a step size of 1 deg. Hence, the illuminated blade had 18 revolutions between every image.

Based on 500 images, each of them illuminated during  $50 \mu\text{s}$ , a mean gray value distribution was calculated to identify the statistical mean cavity on the leading edge of the blade.

The standard deviation of the gray values or its variance can serve as a quantity to determine the unsteadiness of the cavitation. In regions of these images with higher values of the variance (to be identified as dark regions), the fluctuations of the gray values and, therefore, the fluctuations of the reflecting vapor structures are larger than in regions with a smaller variance. Those regions are constantly filled with either water or vapor. The result of such a treatment is shown in Figs. 5 and 6.

Mean distribution (Figs. 5(a) and 6(a)): The attached part of the cavitation can only be identified by its two-phase interface, because the light is mainly reflected. But the mean region with a cloud shedding is also indicated by a higher mean gray value just downstream of the closure region of the cavitation sheet. For the comparison with numerical results, we just identify the attached part. As expected, the extent of both regions enlarges with decreasing NPSH value. As already mentioned, the flow has the tendency to separate at the leading edge of the blade, which is enhanced (Fig. 6(a)) at lower pressure conditions.

Standard deviation (Figs. 5(b) and 6(b)): The fluctuation of the shedding becomes larger with decreasing NPSH and its extension fills almost half of the height of the channel. This is a result of the higher production of transient vapor structures from the leading edge cavitation. In contrast, the interface of the attached cavitation seems to be rather stable. Probably the flow is clearly separated

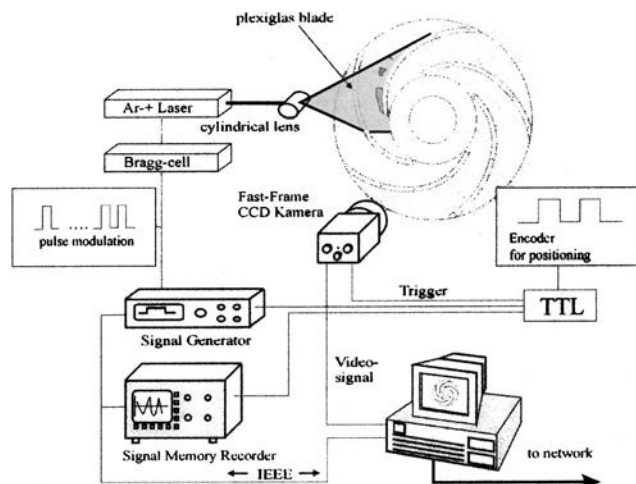


Fig. 2 Visualization setup

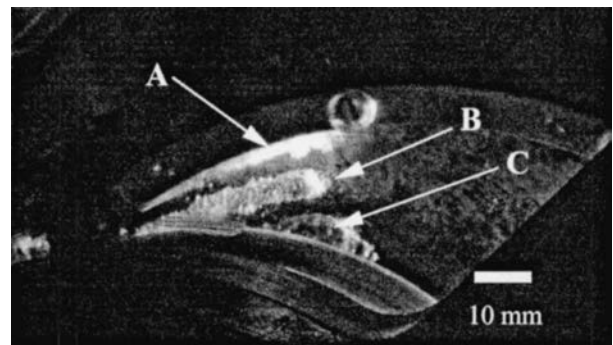


Fig. 3 Unsteady-state of blade cavitation on suction side, NPSH=8 m, stroboscopic light illumination (a scaling bar is added to each image, representing a length of 10 mm)

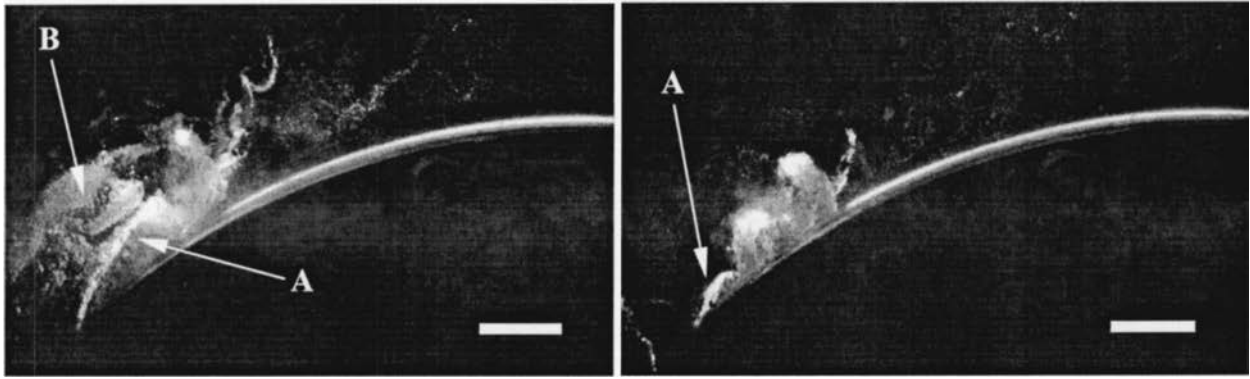


Fig. 4 Unsteady-state of blade cavitation on pressure side at two different time and NPSH=7 m (laser light sheet)

from the leading edge, the separation zone is almost steadily filled with vapor, and only in the closure region vapor is shed into the channel.

#### 4 Physical and Numerical Model

The main features of the physical and numerical models applied to simulate the flow field in the pump are summarized in the present paper. More details are given in [13,14,17].

Cavitating flows are described by a single-fluid model, based on previous numerical and physical work developed at LEGI, [9,18]. This fluid is characterized by a density  $\rho$  that varies in the computational domain: when the density in a cell equals that of the liquid ( $\rho_l$ ), the whole cell is occupied by liquid, and if it equals that of the vapor ( $\rho_v$ ), the cell is full of vapor. Between these two extreme values, a liquid/vapor mixture, still considered as one single fluid, occupies the cell. The void fraction  $\alpha = (\rho - \rho_l) / (\rho_v - \rho_l)$  can thus be defined as the local ratio of vapor contained in this homogeneous mixture.

Velocities are assumed to be locally the same for liquid and for vapor. An empirical state law is used to manage the mass fluxes resulting from vaporization and condensation processes. That barotropic law links the density to the local static pressure  $\rho(P)$ . When the pressure is remarkably higher or lower than vapor pressure, the fluid is supposed to be purely liquid or purely vapor, according to the Tait equation or to the perfect gas law, respectively. The two fluid states are joined smoothly in the vapor-pressure neighborhood. This results in the evolution law presented

in Fig. 7, characterized mainly by its maximum slope  $1/A_{\min}^2$ , where  $A_{\min}^2 = \partial P / \partial \rho$ .  $A_{\min}$  can thus be interpreted as the minimum speed of sound in the mixture.

The numerical model of cavitating flows based on that physical description is generated on the basis of the commercial code FINE/TURBO™ developed by NUMECA International. FINE/TURBO™ is a three-dimensional structured mesh code that solves the time dependent Reynolds-averaged Navier-Stokes equations. Time-accurate resolutions of the equations use the dual-time stepping approach. Pseudo-time derivative terms are added to march the solution towards convergence at each physical time-step. The range of application is extended to weakly compressible or incompressible flows by introducing a preconditioning matrix, [19]. The discretization is based on a finite volume approach. Convection terms are treated by a second-order central scheme associated with artificial dissipation terms. The pseudo-time integration is made by a four-step Runge-Kutta procedure. The physical time-derivative terms are discretized with a second-order backward difference scheme. The code resorts to a multigrid strategy to accelerate the convergence, associated with a local time-stepping and an implicit residual smoothing.

The numerical model was adapted to treat the cavitation process, [13,17]. The key point of this adaptation is the modification of the state law of the fluid. Applied barotropic law implies the simultaneous treatment of two different cases: the fluid is highly compressible in the liquid/vapor mixture (the Mach number can be as high as 4 or 5) and is almost incompressible in the pure



Fig. 5 Mean vapor distribution and standard deviation on pressure side, Qn, NPSH=7 m



Fig. 6 Mean vapor distribution and standard deviation on pressure side, Qn, NPSH=6 m

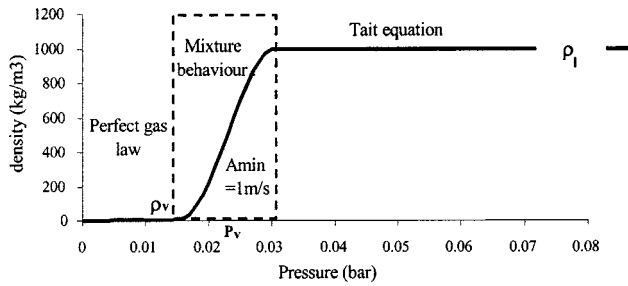


Fig. 7 The barotropic state law  $\rho(P)$  for water

vapor or pure liquid areas. So the main difficulty consisted in managing these two different states of the fluid, without creating any spurious discontinuity in the flow field. Besides, cavitation consists in a very sharp and very rapid process. The density variations in time and space are smoothed to avoid numerical instabilities. This under-relaxation of density implies that a minimum number of pseudo time-steps must be imposed within each physical time step to avoid any effect of this parameter on the result.

More details concerning the basic numerical method can be found in [20], and a more precise investigation of the influence of numerical parameters in cavitating conditions (artificial dissipation, turbulence model, physical time step, mesh size . . . ) is available in [17].

The model was applied to the presented centrifugal pump geometry. Several meshes were tested, as well H-I typed as H-O typed, including between 300,000 and 700,000 cells. They are composed of two blocks (the impeller and the inlet domain) in the H-I case, and three blocks (the inlet domain, the impeller, and the outlet domain) in the H-O case. Only one blade-to-blade channel is treated, and periodicity conditions are applied to the frontiers

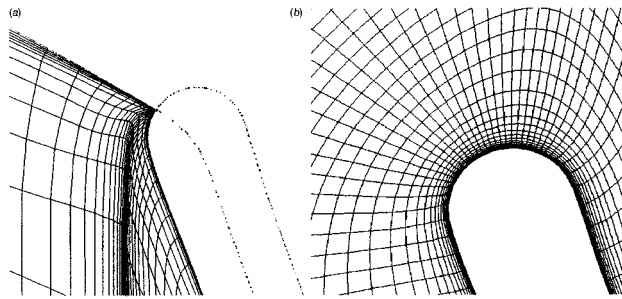


Fig. 8 Mesh of the leading edge with (a) a H-I type mesh, (b) a H-O type mesh

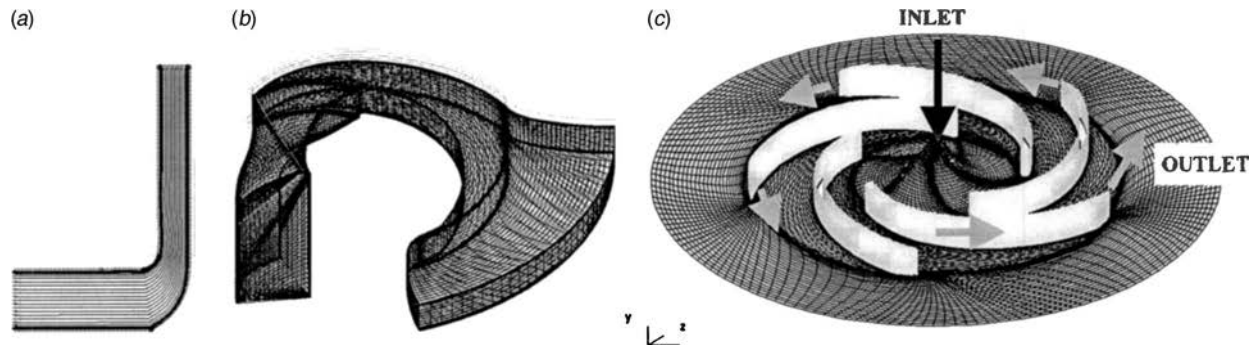


Fig. 9 Mesh applied for the calculations (300,000 cells). (a) Meridional view, (b) three-dimensional view of a blade-to-blade channel, (c) view of the mesh on hub side of the pump. (The entire pump geometry is reconstructed by rotation of the single blade-to-blade channel.)

with the adjacent channels. This automatically implies that the five channels will behave the same way during the numerical simulation.

H-O meshes are particularly well adapted to the present geometry, because of the sharp leading and trailing edges (Fig. 8). H-I meshes induce more important stretchings of the cells in these areas, but they also lead to more reduced mesh sizes.

Noncavitating steady calculations were performed with the different meshes, and the results showed the weak influence of the mesh type on the pump performance and on the pressure field around the leading edge. Consequently, all the simulations presented hereafter were obtained with the H-I 300,000 cells mesh, whose structure is presented in Fig. 9. Special attention was paid to the cavitating areas (suction side of the blade, leading edge . . . ): the stability study reported in [17] shows indeed that cells characterized by a high distortion or high aspect ratio strongly penalize the numerical stability in cavitating conditions. Thus, a fine grid is applied in these areas. Figure 9 hereafter shows the radial mesh structure, a three-dimensional view of a complete blade-to-blade channel, and some details of the mesh on the hub surface.

Conditions applied for the simulations are the following:

- Turbulence model: we use for the simulations presented in this paper a Baldwin-Lomax turbulence model. A more detailed study of the influence of the turbulence model on two-dimensional unsteady cavitation simulation is proposed in [21] and [22]. Those works pointed out a major influence of the compressibility effect modeling on the unsteady behavior of cloud cavitation. Other three-dimensional calculations considering different  $k-\epsilon$  turbulence models are in progress to improve the physical analyses.
- Boundary conditions (Fig. 10): velocity is imposed at the inlet of the suction pipe. Laws of the wall are imposed along solid boundaries. The relative motion between the inlet pipe walls and the impeller is taken into account. On the other hand, the outlet housing shape is not described and the parallel walls are treated as hub and shroud extensions up to the outlet, at 1.5 times the impeller outer radius, where a uniform static pressure is imposed.
- Initial transient treatment: First of all, a steady step is carried out, with a pseudo vapor pressure low enough to ensure non-cavitating conditions in the whole computational domain. Then, the NPSH is slowly lowered by increasing smoothly the pseudo vapor pressure at each new time-step up to the physical value. Vapor structures spontaneously appear and grow during that process, in the regions of low static pressure. The final NPSH value, depending on the outlet static pressure imposed, is then kept constant throughout the computation.

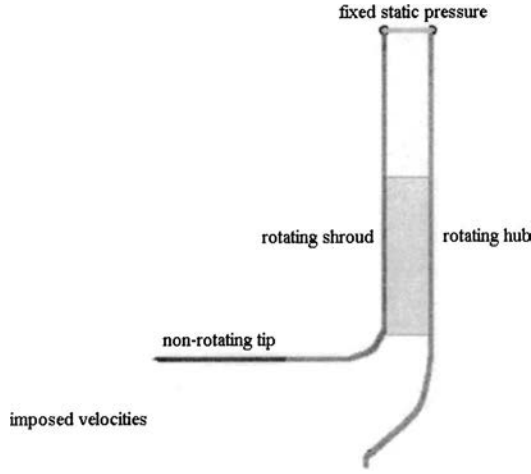


Fig. 10 Boundary conditions

## 5 Noncavitating Characteristics

Experimental tests and numerical calculations were performed considering a large range of flow-rates, in non-cavitating conditions. Figure 11(a) illustrates the computational result at nominal flow rate: the total pressure distribution is represented at half-width of the pump channels. Figure 11(b) presents a comparison between the numerical and experimental performance charts. Directly based on the measurements performed, the head of the pump is defined as the difference between downstream static pressure and upstream total pressure.

$$H = \frac{p_{\text{outlet}} - p_{\text{tot}}^{\text{inlet}}}{\rho g}$$

where  $p_{\text{tot}}^{\text{inlet}} = p_{\text{inlet}} + \frac{\rho V_{\text{inlet}}^2}{2}$

$p_{\text{inlet}}^{\text{inlet}}$  and  $p_{\text{outlet}}$  are the static pressures measured, respectively, at the pump inlet and outlet, and  $V_{\text{inlet}}$  is the mean inlet velocity. The outlet pressure was determined by taking the static wall pressure in the vaneless diffuser at 5 static pressure taps located at a diameter of 500 mm and averaged by connecting all pressure taps to a single pressure transducer.

The total pressure at pump inlet is determined from the wall pressure and the velocity head two diameters upstream of pump

inlet where the velocity is calculated from measured flow rate and the area of the measuring cross section. Precise locations of the sensors in the experiments are consistent with the inlet and outlet of the computational domain in the calculation.

We observe a reliable agreement between the pump characteristics given by measurement and computation in the whole range of flow rates investigated experimentally. The model gives a better prediction when the flow rate is over 50 percent of the nominal value ( $Q_n = 210 \text{ m}^3/\text{h}$ ), and the numerical simulation becomes unstable at very low partial flow rate. As a matter of fact, the numerical simulation slightly overestimates the pump head. This is an expected result, since the flow through the side chamber is not taken into account in numerical simulations. This gap flow of the pump impeller has to be added to the flow rate actually passing through the blade-to-blade channels and is therefore slightly higher in the experiments than in the model. At nominal flow rate, the head is overestimated by about 5 percent (40.5 m instead of 38.5 m). The uncertainty of the measured value was estimated to be no more than 0.8 m and corresponds to 2 percent of the value, which also has to be taken into account.

## 6 Cavitation Behavior

Numerical simulations of the pump are performed in cavitating conditions at several flow rates. First, we present some qualitative results, consisting in a visualisation of the vapor/liquid structures inside the pump at nominal flow rate and for several NPSH values. Then, a quantitative analysis is performed, using the experimental results: head drop charts are studied at three flow rates, and the shape of the cavitating areas at nominal flow rate is compared to visualisations inside a blade-to-blade channel.

**6.1 Qualitative Results.** The head drop chart  $H(\text{NPSH})$  obtained by the calculation at nominal flow rate is drawn in Fig. 12. The green line corresponds to the apparition of vapor in the flow field. The six blue points indicated on the chart are related to the six visualisations of the cavitating flow field presented in Fig. 13 and 14 hereafter. The quantity NPSH has the following definition:

$$\text{NPSH} = \frac{p_{\text{tot}}^{\text{inlet}} - p_{\text{vap}}}{\rho g}$$

where the inlet total pressure was defined previously.

The head drop is only partially obtained by the computation: this point will be discussed hereafter.

Figures 13 and 14 show the development of cavitation corresponding to the six operating conditions indicated on the chart. Figure 13 illustrates the apparition and the growing of vapor/

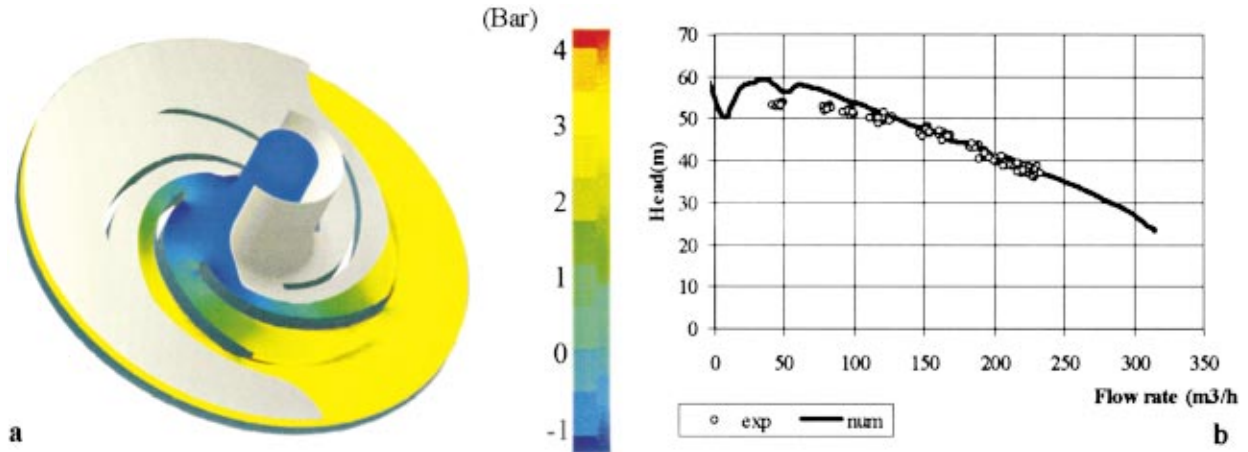
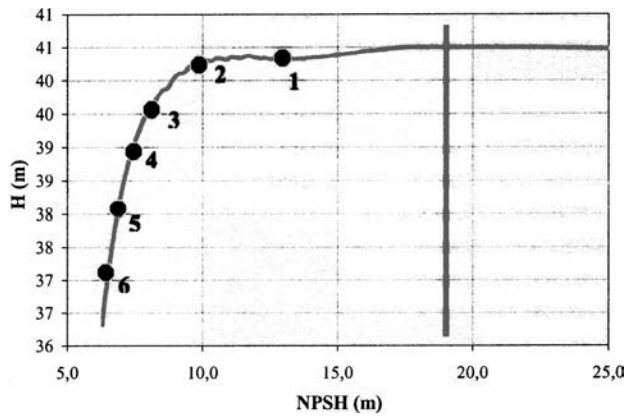


Fig. 11 (a) Total pressure elevation in the pump (nominal flow rate), (b) characteristics  $H(Q)$  of the pump in noncavitating conditions



**Fig. 12 Head drop chart at nominal flow rate. The points indicate the cavitating conditions visualized on Figs. 13 and 14. The line corresponds to the apparition of vapor.**

liquid areas on both faces of the blades, and finally the progressive filling of blade-to-blade channels by the vapor. Blades are colored in gray, the shroud in blue, and the external shape of the two-phase areas (corresponding to a 5 percent void ratio) is colored in yellow.

We observe that cavitation appears first on the suction side (Fig. 13-1), and also quite rapidly on the pressure side (Fig. 13-2). The vapor volume increases mainly on the suction side (Figs. 13-3 and 13-4). A vapor structure also grows on the shroud, in the vicinity of the inlet, caused by the local curvature of the streamlines. It progressively joins the attached cavity on the blade.

The pressure side cavity is almost uniform from hub to shroud, and it grows slowly as the NPSH decreases. On the contrary, the suction side cavitation remains very close to the shroud, where the obstruction is mainly visible (Figs. 13-5 and 13-6).

For a better understanding of the liquid/vapor mixture behavior in the pump, we have presented on Fig. 14 the void ratio distribution on a blade-to-blade surface, close to the shroud. The velocity field is also drawn in each case. It indicates the void ratio variations in the suction side cavity, and in the two-phase areas observed on the shroud.

We observe that the void ratio obtained on the suction side of the blade increases rapidly: it reaches almost 90 percent in the

second configuration, in the middle of the attached cavity. On the contrary, the vapor region on the shroud is characterized by a low void ratio, which reaches only 60 percent, and the cavity on the pressure side of the blades is mainly composed of liquid, even when its volume increases. That low void ratio is probably related to fluctuations of the vapor/liquid structures, which are not obtained by the simulation. It is worth noting that we use here a high time-step ( $\Delta t = 10^{-4}$  s, i.e. 1/300 of one rotation period), so that the unsteady phenomena are not modeled, and a quasi-static head-drop chart can be obtained. As a consequence, each operating point represented here corresponds to a mean flow field that does not take into account the eventual instabilities generated by cavitation.

**6.2 Comparisons With Experiments.** Numerical simulation of the cavitation characteristics of the pump was performed at different flow rates. The shape of the cavitating structures is first compared to the experimental visualisations presented above at nominal flow rate. When the NPSH decreases in the calculation, attached cavitation sheets grow both on the suction side and on the pressure side, as observed experimentally. Moreover, vapor structures appear at the inlet radius of the shroud. This cavitation behavior is fully consistent with the observations reported previously. The visualisation obtained in Fig. 3 is compared to the computational results to enhance the reliable agreement. The cavitation number was adjusted to give the same global extent of the cavitation structures as in the experiment: the numerical result then corresponds to a NPSH about 10 percent lower than the experimental one (7 m, instead of 8 m). The three cavitation areas are correctly simulated by the code (Fig. 15): attached cavity on the suction side (A), extent of cavitation on the shroud along the blade (B), and cavitating flow on the inlet radius of the shroud (C). In the computation, attached sheet cavity (A) and extent on the shroud (B) belong to the same vapor structure, while they look like two separated regions in the experiment.

Figure 16 shows the attached cavity on the pressure side of the blade. Its size is compared to the mean distribution obtained from gray level averaging (Fig. 5). Both experimental and numerical NPSH values are equal to 7 m. Here, the calculated cavity appears smaller than the experimental one. Moreover, only the steady attached part of the cavity on the pressure side is obtained by the computation. The transient vapor structures in the unsteady cavity closure region are not found from the simulation. Actually this is still a limitation of the physical and numerical model. The mesh

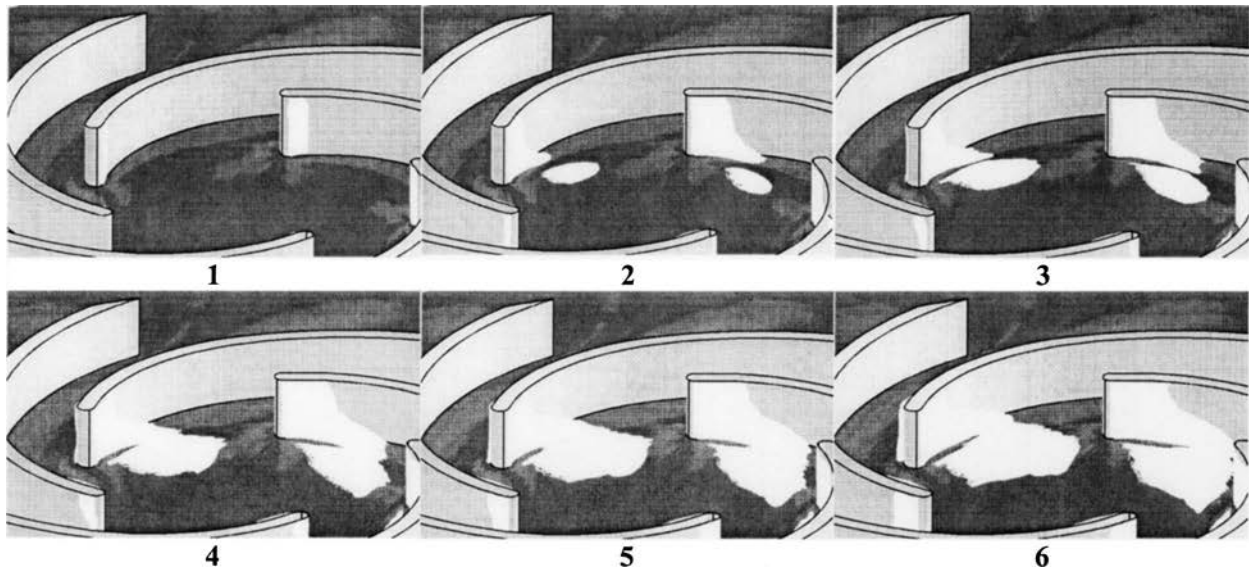


**Fig. 13 Development of the two-phase areas as NPSH decreases (corresponding to points on Fig. 12)**

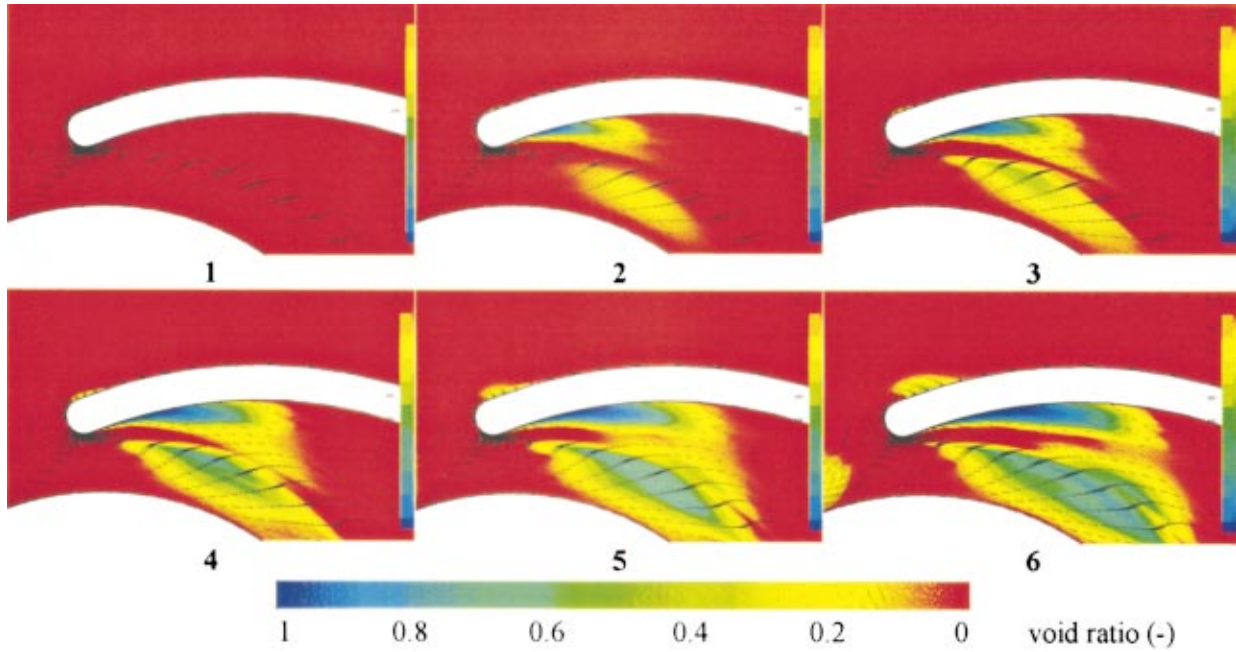


Fig. 14 Void ratio evolution on a blade-to-blade surface close to the shroud, and velocity fields (corresponding to the NPSH decrease represented on Fig. 12)

size and the standard turbulence model used in the calculation do not allow catching the cloud shedding process downstream of the attached cavity. An ongoing work is pursued to improve this aspect.

In Fig. 17, we summarize the whole comparison, by drawing the head drop curves for three different flow rates: namely  $0.8Q_n$ ,  $Q_n$  and  $1.08Q_n$ . In non-cavitating conditions, we observe again a slight overestimation of the pump head (about 5 percent at nominal flow rate), mainly due to the fact that the gap flow through the side chamber is not considered in the simulation. From the numerical point of view, while decreasing the NPSH, the performance drop appears first as a smooth decrease of the pump head. The final head-drop is only partially simulated because the computation rapidly becomes unstable and stops (this is more particularly the case at  $1.08Q_n$ ). Our upstream boundary condition consists in imposing in a strict manner the mass flow rate passing the pump. Because the coupling between the pump and the hydraulic loop is not taken into account, the effects of the cavitation blockage on the flow rate are neglected and the head-drop is less pro-

gressive than in the experiments. However, all the numerical results represented in Fig. 17 refer to a converged solution at the corresponding physical time-step.

Results obtained from first simulations of the pump cavitation behavior are promising: the head drop is predicted with a good homogeneity with respect to the 3 flow rates. The NPSH values obtained for the 3 percent and 10 percent head drop are globally overestimated in respect to experimental values (of about 1 m for the 10 percent head drop, and 1.5 to 3 m for the 3 percent head drop, see Fig. 18). These results correspond to our first try of predicting the cavitation characteristic of a pump, and a study of the effect of the model parameters (mainly the turbulence model) might probably improve the quantitative agreement.

It can be observed that the head measured in experiments increases a little bit in low conditions before the head drop, for the three flow rates. This effect is not obtained in the calculations. However, it does not exceed 1 to 2 percent of the initial head, whereas the discrepancy between calculations and experiments concerning the pump performance is about 2 to 5 percent. More-

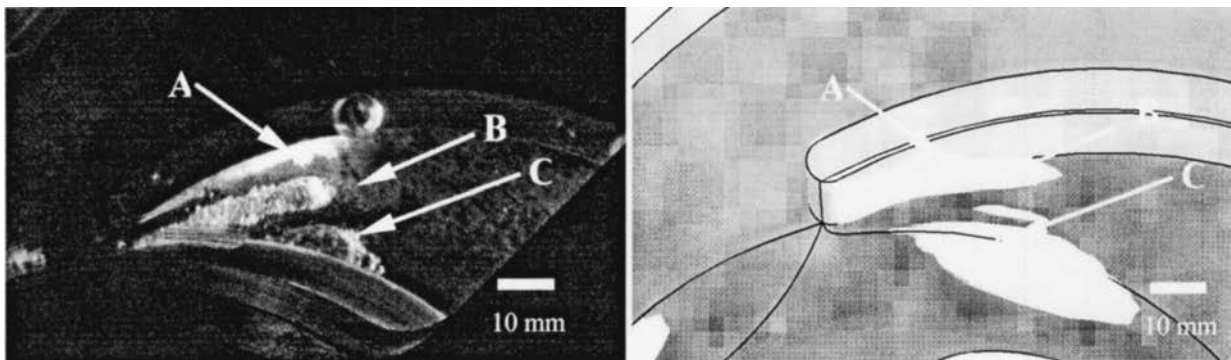


Fig. 15 Vapor structures on suction side (experiment NPSH=8 m, computation NPSH=7 m). Calculation: iso-density contour ( $\rho \approx 0.95\rho_1$ : void ratio >5 percent) drawn in yellow, shroud in blue, blade in gray.

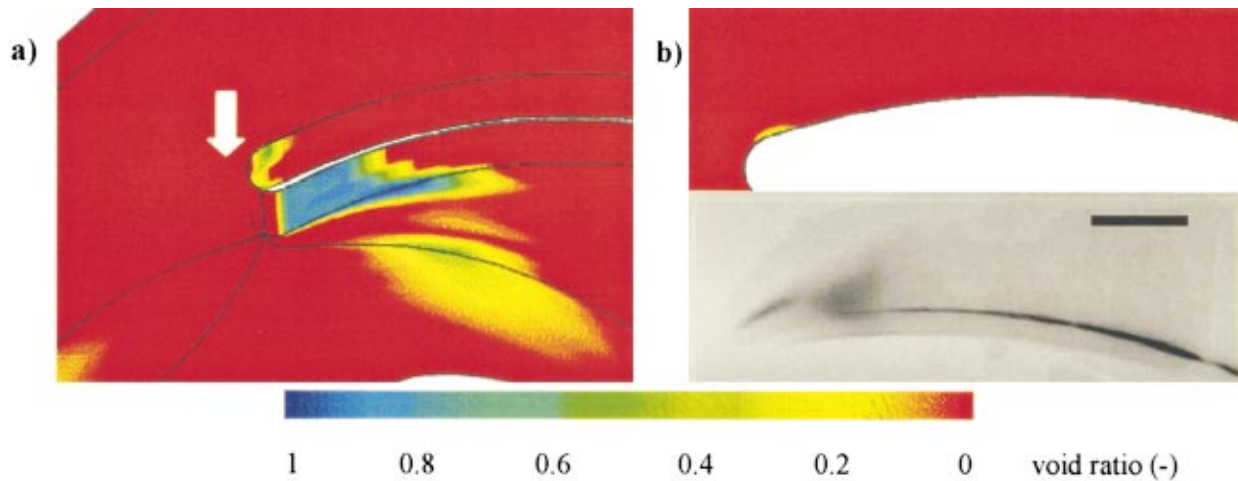


Fig. 16 (a) Numerical void ratio distribution, (b) pressure side cavity, comparison with experiment (NPSH=7 m)

over this effect, which has been observed also in the case of turbopump inducers [17], is not yet well explained, may be due to a coupling between the pump channels; such a phenomenon can not be predicted here because only one channel is considered. It probably involves slight interactions between the cavities and the boundary layer along the blade sides, which are not simulated with a sufficient accuracy by our simple turbulence model.

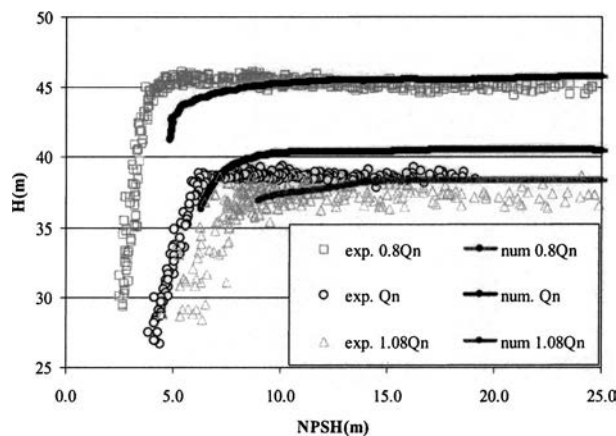


Fig. 17 Head-drop curves in cavitating conditions: comparison at  $0.8 Q_n$ ,  $Q_n$ , and  $1.08 Q_n$ .

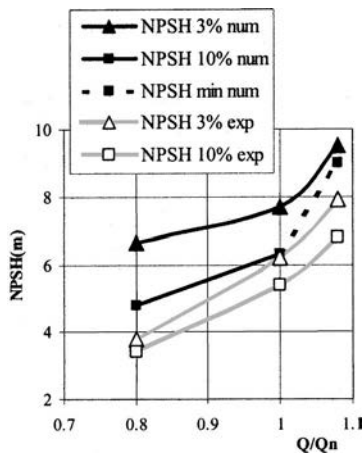


Fig. 18 NPSH values for 3 percent and 10 percent head drop

## 7 Conclusion

Numerical and experimental results were presented in this study, concerning a test pump having an impeller with 2D curvature blade geometry.

From the experimental point of view, besides the measurements of the cavitation characteristics of the pump in various conditions, a special visualisation set-up was developed to investigate the unsteady behavior of leading edge cavitation. Image processing and statistical treatment of the photographs taken at given impeller position allowed to quantify the attached and cloud cavitation extent.

A numerical model of three-dimensional cavitating flows, based on the three-dimensional code FINE/TURBO™, has been developed to predict the cavitation behavior in turbomachinery, [13,14]. This model was applied to the centrifugal pump geometry. Non-cavitating and cavitating conditions were investigated. Calculations were found to be in good agreement with experimental measurements and visualisations. Experimental and numerical results concerning the pump characteristics and performance breakdown were drawn at different flow conditions and the mean spatial distributions of vapor structures within the impeller were compared: It was found that the main features of the cavitating flow field are correctly simulated by the model. These results show the ability of the model to simulate the complex three-dimensional development of cavitation in rotating machinery, and the associated effects on the performance. This is of first importance for the purpose of pump future design. However, the fluctuating two-phase areas are not simulated yet, and work is in progress to improve the numerical model in that way. This is a necessary further step to predict more efficiently the local void ratio, since its distribution usually slightly evolves when unsteady effects are correctly predicted, [18]. The final objective is to simulate the unsteady effects due to cavitation (cavity self-oscillation, rotating cavitation) in three dimensions, as we already performed in more simple two-dimensional configurations, [4,23].

## Acknowledgments

This work is part of a European exchange program PROCOPE with the research teams of Grenoble and Darmstadt as members. The numerical cavitation model implemented in FINE/TURBO™ has been developed with the support of SNECMA Moteurs DMF (Rocket Engine Division), and the French space agency CNES. The experimental work carried out at Darmstadt was part of the research project STO 190/9-2 which was financially supported by the DFG (German Research Foundation).

## Nomenclature

- $A_{\min}$  = minimum speed of sound in the mixture (m/s)  
 $H$  = pump head =  $(P^{\text{outlet}} - P^{\text{inlet}}) / \rho_1 g$  (m)  
 NPSH = net positive suction head =  $(P^{\text{inlet}} - P_{\text{vap}}) / (\rho_1 g)$  (m)  
 $P$  = local static pressure (Pa)  
 $P_{\text{tot}}$  = total pressure =  $P + \frac{1}{2} \rho_1 V^2$  (Pa)  
 $P_{\text{vap}}$  = vapor pressure (Pa)  
 $P^{\text{inlet}}$  = static pressure measured in the inlet pipe (Pa)  
 $P^{\text{outlet}}$  = static pressure measured at  $r \approx 1.5 r^{\text{outlet}}$  (Pa)  
 $Q, Q_n$  = flow rate, nominal flow rate ( $\text{m}^3/\text{s}$ )  
 $r$  = local radius (m)  
 $r^{\text{outlet}}$  = radius at the impeller outlet (m)  
 $t, \Delta t$  = time, time-step (s)  
 $V$  = local velocity (m/s)  
 $V_{\text{inlet}}$  = inlet mean velocity (m/s)  
 $\alpha$  = local void fraction  
 $\rho$  = local density of the mixture =  $\alpha \rho_v + (1 - \alpha) \rho_1$  ( $\text{kg}/\text{m}^3$ )  
 $\rho_1$  = liquid density ( $\text{kg}/\text{m}^3$ )  
 $\rho_v$  = vapor density ( $\text{kg}/\text{m}^3$ )

## References

- [1] Lohrberg, H., Hofmann, M., Ludwig, G., and Stoffel, B., 1999, "Analysis of Damaged Surfaces. Part II: Pit Counting by 2D Optical Techniques," *Proc. of the 3rd ASME/JSME Joints Fluids Engineering Conference*, July, San Francisco, CA, ASME, New York.
- [2] Patella, R., Fortes, Reboud, J. L., and Archer, A., 2000, "Cavitation Mark Measurements by 3D Laser Profilometry," *Wear*, **246**, pp. 59–67.
- [3] Hofmann, M., Lohrberg, H., Ludwig, G., Stoffel, B., Reboud, J.L., and Fortes-Patella, R., 1999, "Numerical and Experimental Investigations on the Self-Oscillating Behavior of Cloud Cavitation: Part 1 Visualisation/Part 2 Dynamic Pressures," *3rd ASME/JSME Joint Fluids Engineering Conference*, San Francisco, CA, July, ASME, New York.
- [4] Lohrberg, H., Stoffel, B., Fortes-Patella, R., Coutier-Delgosha, O., and Reboud, J. L., 2002, "Numerical and Experimental Investigations on the Cavitating Flow in a Cascade of Hydrofoils," *Exp. Fluids*, accepted for publication.
- [5] Takasugi, N., Kato, H., and Yamaguchi, H., 1993, "Study on Cavitating Flow Around a Finite Span Hydrofoil," *Cavitation and Multiphase Flow Forum*, ASME, New York, ASME-FED-vol. 153, pp. 177–182.
- [6] Alajbevoic, A., Grogger, H., and Philipp, H. 1999, "Calculation of Transient Cavitation in Nozzle Using the Two-Fluid Model," 12th Annual Conf. on Liquid Atomization and Spray Systems, May 16–19, Indianapolis.
- [7] Kunz, R., Boger, D., Chyczewski, T., Stinebring, D., and Gibeling, H., 1999, "Multi-Phase CFD Analysis of Natural and Ventilated Cavitation About Submerged Bodies," *3rd ASME/JSME Joint Fluids Engineering Conference*, San Francisco, CA, ASME, New York.
- [8] Bunnell, R. A., and Heister, S. D., 2000, "Three-Dimensional Unsteady Simulation of Cavitating Flows in Injector Passages," *ASME J. Fluids Eng.*, **122**, pp. 791–797.
- [9] Delannoy, Y., and Kueny, J. L. 1990, "Two Phase Flow Approach in Unsteady Cavitation Modelling," *Cavitation and Multiphase Flow Forum*, ASME, New York, ASME-FED-Vol. 98, pp. 153–158.
- [10] Kubota, A., Kato, H., and Yamaguchi, H., 1992, "A New Modelling of Cavitating Flows: A Numerical Study of Unsteady Cavitation on a Hydrofoil Section," *J. Fluid Mech.*, **240**, pp. 59–96.
- [11] Combes, J.-F., and Archer, A., 2000, "Etude de la cavitation dans la pompe SHF," *Coll. Machines Hydrauliques: Institutionnarités et effets associés*, Société Hydrotechnique de France, Chatou, France.
- [12] Medvitz, R. B., Kunz, R. F., Boger, D. A., Lindau, J. W., Yocum, A. M., and Pauley, L. L. 2001, "Performance Analysis of Cavitating Flow in Centrifugal Pumps Using Multiphase CFD," *ASME Fluids Engineering Division Summer Meeting*, June, New Orleans, LA.
- [13] Coutier-Delgosha, O., Fortes-Patella, R., Reboud, J. L., and Hakimi, N., 2001, "Numerical Simulation of Cavitating Flow in an Inducer Geometry," 4th European Conference on Turbomachinery, Mar. 20–23, Firenze, Italy.
- [14] Coutier-Delgosha, O., Reboud, J.L., and Fortes-Patella, R., 2001, "Numerical Study of the Effect of the Leading Edge Shape on Cavitation Around Inducer Blade Sections," *Proceedings of the 4th Int. Symp. on Cavitation*, Pasadena, CA, June.
- [15] Hofmann, M., 2001, "Ein Beitrag zur Verminderung des erosiven Potentials kavitierender Strömungen," PhD thesis, TU Darmstadt, June.
- [16] Hofmann, M., Stoffel, B., Friedrichs, J., and Kosyna, G. 2001, "Similarities and Geometrical Effects on Rotating Cavitation in 2 Scaled Centrifugal Pumps," *Proceedings of the 4th Int. Symp. on Cavitation*, Pasadena, CA, June.
- [17] Coutier-Delgosha, O., 2001, "Modélisation des Ecoulements Cavitants: Etude des comportements instationnaires et application tridimensionnelle aux Turbomachines," Ph.D. thesis, INPG, Grenoble, France, Nov.
- [18] Reboud, J. L., Stutz, B., and Coutier, O., 1998, "Two-Phase Flow Structure of Cavitation: Experiment and Modelling of Unsteady Effects," *Proceedings of the 3rd Int. Symp. on Cavitation*, Grenoble, France, Apr.
- [19] Hakimi, N., 1997, "Preconditioning Methods for Time Dependent Navier-Stokes Equations," Ph.D. thesis, Vrije Univ., Brussels.
- [20] Hirsch, C., 1990, *Numerical Computation of Internal and External Flows*, John Wiley and Sons, New York.
- [21] Coutier-Delgosha, O., Fortes-Patella, R., and Reboud, J.-L., 2002, "Evaluation of the Turbulence Model Influence on the Numerical Simulations of Unsteady Cavitation," *ASME J. Fluids Eng.*, accepted for publication.
- [22] Coutier-Delgosha, O., Fortes-Patella, R., and Reboud, J.-L., 2002, "Simulation of Unsteady Cavitation With a 2-Equations Turbulence Model Including Compressibility Effects," *J. of Turbulence*, accepted for publication.
- [23] Courtot, Y., Coutier-Delgosha, O., and Reboud, J.-L., 2002, "Numerical Simulation of the Unsteady Cavitation Behavior of an Inducer Blade Cascade," *AIAA J.*, proposed for publication.